Land Surface Temperature

LST is one of the most important climate system variables on a variety of time scales, exerting control over the partitioning of energy into latent and sensible heat fluxes, and a strong indicator of surface warming trends from climate change (Schneider and Hook, 2010).

From: Taking the Temperature of the Earth, 2019

Related terms:

MODIS, Vegetation Index, Brightness Temperature, Sea Surface Temperature, Atmospherics, Emissivity, Air Temperature

View all Topics

Land Surface Temperature

Glynn C. Hulley, ... César Coll, in Taking the Temperature of the Earth, 2019

3.6.1 Introduction

Land Surface Temperature (LST) is a fundamental aspect of climate and biology, affecting organisms and ecosystems from local to global scales. Identified as one of the most important Earth System Data Records by NASA and other international organizations (King, 1999), LST measures the emission of thermal radiance from the land surface where the incoming solar energy interacts with and heats the ground, or the surface of the canopy in vegetated areas. This quality makes LST a good indicator of energy partitioning at the land surface-atmosphere boundary and sensitive to changing surface conditions (Nemani et al., 1996; Wan et al., 2004; Lambin and Ehrlich, 1995; Mildrexler et al., 2009). At spatial scales ranging from the leaf-level to the landscape, the knowledge LST provides on the redistribution of energy into latent and sensible heat fluxes makes it one of the most important parameters in the physical processes of surface energy and water balances (Li et al., 2013; Teskey et al., 2014). Its retrieval from remotely sensed thermal-infrared (TIR) data provides spatially continuous LST measurements with global coverage to examine the thermal heterogeneity of the Earth's surface, and the impact on

surface temperatures resulting from natural and human-induced changes (Jin and Dickinson, 2010; Li et al., 2015).

Daytime LST is more tightly coupled with the radiative and thermodynamic characteristics of the Earth's surface than standard air temperature measurements. LST is also more sensitive to changes in vegetation density and captures additional information on the biophysical controls on surface temperature, such as surface roughness and transpirational cooling (Mildrexler et al., 2011a; Oyler et al., 2016). A growing body of work has demonstrated the utility of LST datasets for ecological and biogeographical studies. Temperatures derived from TIR data have been combined with vegetation indices to separate land cover classes (Lambin and Ehrlich, 1995; Nemani and Running, 1997), monitor land cover dynamics (Julien and Sobrino, 2009) and ecosystem disturbances (Mildrexler et al., 2007, 2009; Coops et al., 2009). Nemani et al. (1993) used LST as an indicator of surface-moisture status, and thermal datasets have been used for monitoring drought and plant stress in agricultural and natural ecosystems (Anderson et al., 2007; Scherrer et al., 2011; Wan et al., 2004; Mildrexler et al., 2016). LST has been used to examine the consequences of land cover changes on climate (Li et al., 2015), and to investigate the association between maximum thermal anomalies, heat waves, melting ice sheets, and droughts in tropical forests (Mildrexler et al., 2018). Thermal data has been used to understand the effects of heat waves on avian community structure (Albright et al., 2011) and habitat usage by koalas (Briscoe et al., 2014).

> Read full chapter

Land Surface Temperature Product from the GOES-R Series

Yunyue Yu, Peng Yu, in The GOES-R Series, 2020

Abstract

Land surface temperature (LST), a legacy (continuity) National Weather Service (NWS) user requirement, is also an essential climate Variable (ECV) required by the Global Climate Observing System (GCOS) of the World Meteorological Organization (WMO). Therefore, LST is produced as one of the baseline products from the Geostationary Operational Environmental Satellites R-Series (GOES-R) mission. It is retrieved from observations of the Advanced Baseline Imager (ABI) thermal infrared channels, using a split-window approach. There are several LST products produced in the GOES-R hourly product package including a full-disk (FD) LST product at 10-km spatial resolution, a contiguous US (CONUS) LST product at 2-km spatial

resolution, and LSTs for two adjustable mesoscale (MESO) sectors (e.g., 1000-km by 1000-km region) at 2-km spatial resolution. Comprehensive evaluation of GOES-16 LST products has been performed using visual inspection, in situ validation, and cross-satellite comparison analyses. The products meet the mission requirement of 2.5 K in accuracy and 2.3 K in precision, in most cases of the validation. Validation of a longer time series of data sets with multiyear seasonal and annual variations are needed to further evaluate the product's performance. This chapter details the LST product quality and its current status.

> Read full chapter

Surface Temperatures in the Urban Environment

Bénédicte Dousset, ... Glynn C. Hulley, in Taking the Temperature of the Earth, 2019

7.2.2.1 Relation Between Land Surface Temperature and Surface Air Temperature

LST and air temperature ($Tair$) are intrinsically distinct yet complementary because the temperature difference between the surface and the air directly above it determines the sensible heat flux, and their correlation arises from the surface heat balance. Fig. 7.11A displays the collocated LST, hourly $Tair$, and relative humidity (RH) at the Paris weather station in Montsouris Park from August1–13. LST and $Tair$ minima occur before sunrise at ~ 05:00 UTC, just before insolation resumed and net radiation ceased to be negative. At night, LST was usually 1–2°C lower than $Tair$ aside from August 12 when the near-surface gradient reached 5°C, probably because of lack of mixing. Maximum LSTs occur at the time of maximum solar irradiance, while maximum $Tair$ typically lags by ~ 3 hours. At ~ 13:00 UTC LST is 2–4°C higher than $Tair$, which implies a significant near-surface temperature gradient due to intense radiative heating (lower LSTs at mid-day August 7–9 are due to lack of data). Some residual discrepancies may be attributable to satellite viewing and anisotropic effects. Fig. 7.11B and C show the night and day correlation of LST and $Tair$ for August 1–13. The linear coefficient was 0.92 at night but 0.68 during the day, presumably reflecting stronger subpixel variations of surface cover and heat balance regimes.
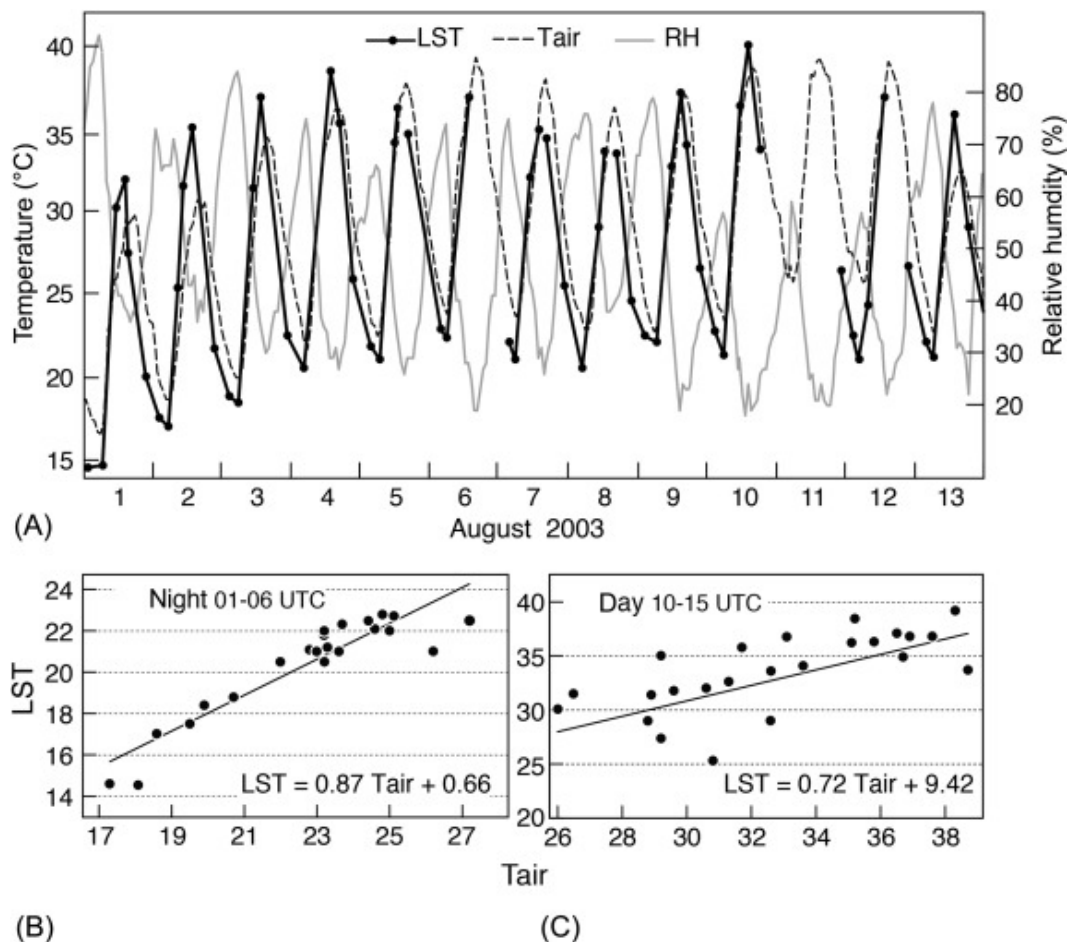
Fig. 7.11. Collocated satellite and in situ data at the Paris weather station in Montsouris Park: (A) LST at the 4–6-hour satellite sampling intervals, hourly *Tair* and hourly RH at 1.50 m, mid-day LST appears lower than Tair for August 5–8 due to a lack of data; (B) scatter plots of LST versus *Tair* at night (01–06 UTC); and (C) at daytime (10–15 UTC) for August 1–13.Reproduced from Dousset, B., Gourmelon, F., Laaidi, K., Zeghnoun, A., Giraudet, E., Bretin, P., Mauri, E., Vandentorren, S., 2011. Satellite monitoring of summer heat waves in the Paris metropolitan area. Int. J. Climatol. 31, 313–323, with permission from John Wiley & Sons.

> Read full chapter

Continental Scale Monitoring of Sub-daily and Daily Evapotranspiration Enhanced by the Assimilation of Surface Soil Moisture Derived from Thermal Infrared Geostationary Data

N. Ghilain, in Satellite Soil Moisture Retrieval, 2016

3.3 Prototype Usage of Soil Moisture Products

Land surface temperature is not a universal indicator of soil moisture. Past studies (Prigent et al., 2005) discovered that the amplitude of the land surface temperature diurnal cycle was related to soil moisture in regions controlled by thermal inertia, not in transpiration-driven regions (Teuling et al., 2009). The validation study presented in Ghilain et al. (2015) exhibits the same conclusions: results from the comparison show an overall good performance over semiarid regions and degradation toward more wet and vegetated areas. As an operational application should not be of degraded quality by a change in the model or in its settings, a comparison of the performances of the two sources was undergone over Africa and Europe to select the best source of soil moisture data in function of climate zones. One of the indicators used in this comparison with observational ground-truthing data sets was the correlation coefficient, which is one of the measures of soil moisture products quality requested by the EUMETSAT users (http://hsaf.meteoam.it/documents/docs/20130100/SAF_HSAF_CDOP2_PRD_1_0.pdf). By grouping the results of the statistical comparison for the different sites within a climate zone, it was possible to state the actual performance of the two sources, and to define where the soil moisture derived from Meteosat satellite data could better characterize soil moisture than ECMWF IFS forecasts for days with not completely overcast conditions (see Fig. 7). The interpretation of the diurnal variation of LST in terms of soil moisture is further hampered by the specific viewing geometry of the SEVIRI sensor and its relation to terrain orography. Areas with complex terrain are assigned to ECMWF IFS soil moisture, as more research would be needed to disentangle the signal from the soil moisture from its perturbation due to shadows and facing south observation. In the Mediterranean region, scores of the ECMWF IFS are slightly higher than the thermal signal from the satellite. But, as irrigation is a common agricultural practice in that zone, and ECMWF IFS does not perform up to now to a spatial resolution where irrigation may have an impact on weather, we select the thermal signal for soil moisture primary source in the regions where irrigation is significant (at least 10% based on the cadastral map of agricultural infrastructure (Siebert et al., 2010, 2013) and the available data from the Food and Agriculture Organization).
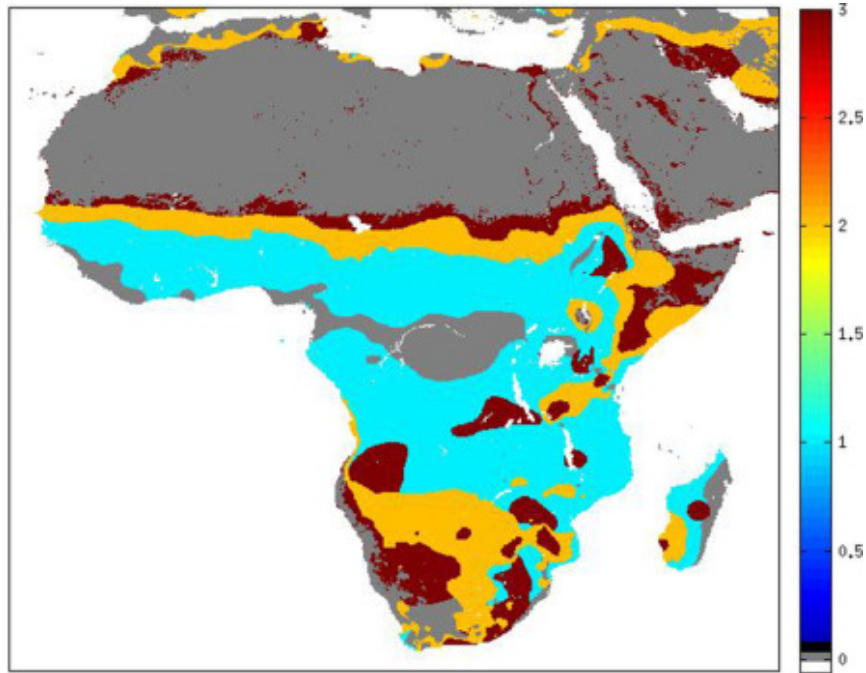
Fig. 7. Map of choice of input data for soil moisture based on the clustering by climate of comparison of both sources to in situ observations: EO derived is best based on correlation *(brown areas)*, ECMWF IFS is best *(light blue)*, equal/slightly better ECMWF IFS (within 3% difference in correlation) *(orange)*, and unknown accuracy *(grey)*. The best source possible is used by the LSA-SAF ET new prototype.

Finally, for regions where the primary source is the satellite-derived soil moisture, unavoidable gaps due to persistent cloudy conditions or to missing satellite data are filled by ECMWF IFS soil moisture, locally adapted to match the temporal dynamics imposed by the soil moisture derived from the satellite (Liu et al., 2011) (see Fig. 8).
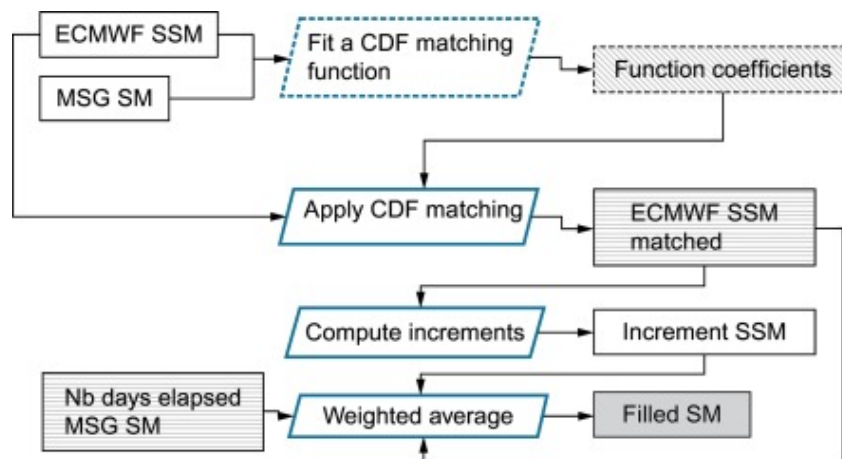

Fig. 8. Flowchart of the process of filling gaps due to persistent cloud coverage in time series of soil moisture derived from LST. ECMWF IFS soil moisture is matched to past series and coefficients are applied to transform it when needed.

Once a surface soil moisture map has been obtained, the root-zone soil moisture is computed for zones with prevalence of the satellite input using an exponential filter (Albergel et al., 2008), differentiated for high and low vegetation types. For zones

where ECMWF IFS is selected as the primary source for soil moisture, nothing is altered in the algorithm exposed in the first section.

> Read full chapter

Vulnerability to Heat Waves, Floods, and Landslides in Mountainous Terrain

Maria Papathoma-Köhle, ... Unni Eidswig, in Assessment of Vulnerability to Natural Hazards, 2014

8.4.2 Vulnerability Assessment Methodology for Heat Waves

The case study focuses on the social dimension of vulnerability. To establish the impact of heat waves on the citizens of Bolzano, it seemed most reasonable to focus on subgroups that are most susceptible to heat waves. As already identified by previous studies (Drinkwater and Horvath, 1979; Basu and Samet, 2002), these are the elderly.

Spatial exposure and social vulnerability were assessed by using the following methods:

1.   Remote sensing (Spatial exposure):

Land-surface temperature was derived from the thermal band of various Landsat Images after atmospheric correction in order to receive rough information about temperature distribution within Bolzano. Overall 12 Landsat 5 scenes of summer months (June, July, August, and September) were used for the period 2003–2009 and in each scene the temperature deviation from each pixel to the maximum temperature value of the same scene was calculated.

2.   Statistical analysis (Social susceptibility):

Correlation analysis was carried out by comparing time series of demographic and health-related data with respect to time series of meteorological data. The demographic dataset was split into various subgroups according to age and gender. Hospital emergency/admission data were divided by gender and age in order to focus on different subgroups. Two different age limits were chosen in order to establish a relationship between the climate data and the hospital data for men and women (A) aged 65 and older; and (B) aged 75 and older.

The aim of the statistical analysis was to investigate the correlation between the hospital admissions of the different subgroups and the temperature data in order to find out the most vulnerable population group. A correlation between the two datasets would show the impact of heat stress on the different subgroups and sustain the hypothesis that heat problems are an issue in Bolzano. Therefore, we compared the means of the various subgroups by performing T-tests.

3. Potential heat wave index (Social vulnerability):

A composite indicator was applied which combines different factors, using the semiquantitative fuzzy logic technique (Kropp et al., 2009). This approach allowed for an assessment and comparison of the social vulnerability of the five districts of Bolzano, considering spatial exposure and social susceptibility. Quantitative data provided by the province and the regional hospital of Bolzano were analyzed and visualized with the statistical programming tool R and ArcGIS within the scope of identifying the parts of the city which are more vulnerable than other ones, a comparative vulnerability assessment was then made within Bolzano. This technique has the advantage that variable values are allocated gradually rather than in binary fashion. Thus, a ranking of the districts referring to possible heat wave impacts was created.

4. Stakeholder involvement (Lack of resilience, Risk Governance):

Stakeholders such as responsible for heat waves in civil protection and municipality, experts, health care managers, representatives from volunteer organizations, and spatial planning experts were interviewed. The aim of these interviews was to collect information on awareness issues, experience with heat waves in the recent past, existing monitoring and forecast systems, and information flow issues between different institutions but also media and the population. The interviews may enable the identification of gaps and the possibilities for improvement.

The indicators used for each of the above mentioned approaches are shown in Table 8.3.

TABLE 8.3. Methods and Indicators Used for the Assessment of Vulnerability to Heat Waves

Method	Indicators
Statistical analysis	•Maximum air temperature (exposure)•Number of heat days; i.e., days with $T_{max} \geq 30\ °C$ (exposure)•Number of heat waves, i.e., number of events with three consecutive days of $T_{max} \geq 30\ °C$ (exposure)•Number of tropical nights•Num-

	ber of combined heat days and tropical nights (exposure)•Relative air humidity (exposure)•Combined indicators: the dew point temperature and the heat-index. Both combine temperature and relative air humidity (exposure) (Steadman, 1979-)•Elderly population divided by gender, considering different age classes (≥65-years and ≥75 years) (sensitivity indicator)
Potential heat wave index	•Percentage of impervious area (exposure)•Percentage of area with land-surface temperature >28 °C, derived from Landsat images of July 2003 (exposure)-•Population density (people/km$_2$) (sensitivity)•Population older than 65 years (sensitivity)•Population older than 65-years living alone (sensitivity)
Stakeholder involvement	•Risk monitoring and forecasting: analysis of existing monitoring system•Information flow: analysis of the information flow in case of heat waves (responsible authority for the forecast, involvement of mass media, and dissemination through health care institutions)•Response measures for most vulnerable population groups: through interviews with managers of care homes and volunteer associations•Risk governance: assessment of the procedures of risk governance in the case study areas

> Read full chapter

A Look to the Future: Thermal-Infrared Missions and Measurements

Glynn C. Hulley, ... Simon J. Hook, in Taking the Temperature of the Earth, 2019

8.4 Joint Polar Satellite System (JPSS)

Global LST and emissivity (LST&E) products are produced routinely by NASA and the National Oceanographic and Atmospheric Administration (NOAA) from the Moderate Resolution Imaging Spectroradiometer (MODIS) and Visible Infrared Imager Radiometer Suite (VIIRS) sensors on board Aqua (since 2002)/Terra (since 2000) and Suomi National Polar-Orbiting Partnership (Suomi-NPP) (since 2011) (Justice et al., 2013) platforms using dual data processing streams at moderate spatial resolution (~ 750–1 km) on twice-daily time steps. The Suomi-NPP VIIRS LST product has an overpass time of 1:30 am/pm and bridges the gap between NASA's Earth Observing System (EOS) data derived from the MODIS Aqua sensor since 2002 (King, 1999) and the next generation Joint Polar Satellite System (JPSS-1) platform that was launched on November 2017. A stable and continuous record of LST produced from well-calibrated data and consistent algorithms is critical for monitoring climate trends, reducing systematic biases in land surface models, and for filling gaps where few in situ measurements of surface air temperatures exist (Hulley et al., 2017).

The JPSS is a new generation polar-orbiting environmental satellite system run jointly by the National Oceanic and Atmospheric Administration (NOAA) and NASA. This collaborative effort is the latest generation of US polar-orbiting environmental satellites that will gather global measurements of Earth's atmosphere, oceans, and land through 2038. The first satellite in the JPSS was Suomi-NPP launched on October 28, 2011. This was followed by JPSS-1 (renamed to NOAA-20) that launched on November 18, 2017. Operational continuity will be achieved by launching an additional three other JPSS satellites (JPSS-2, JPSS-3, and JPSS-4) between the 2022 and 2031 nominal timeframes.

The JPSS satellites all contain five instruments, one of which is the VIIRS scanning radiometer that collects visible and infrared imagery of the global land surface twice per day. VIIRS has 22 bands with a spectral coverage from 0.412 to 12 μm. Among 22 bands, there are 5 high resolution imagery channels (I-bands), 16 moderate resolution channels (M-bands), and 1 day/night band (DNB). The I-bands have a spatial resolution of 375 m at nadir and M-bands (and DNB) have a spatial resolution of 750 m at nadir. In the cross-track direction, the scan swath width is ~ 3040 km. The thermal M-bands (M14, M15, M16 at 8.55, 10.6, and 12 μm respectively) acquire data at 750 m resolution across the entire instrument scan (Cao et al., 2014; Hillger et al., 2013; Justice et al., 2013). This is an improvement on the MODIS thermal bands that have a resolution of 1-km at nadir, increasing to 5–6 km at the edge of scan.

In order to maintain continuity between the MODIS-Aqua LST&E product starting from 2002 and VIIRS-SNPP LST&E product starting in 2011, NASA is currently

producing these products for MODIS (MxD21, Collection 6) and VIIRS (VNP21, Collection 1) using a consistent algorithm called the Temperature Emissivity Separation (TES) algorithm, which dynamically retrieves the LST and emissivity for the three thermal bands on each sensor (Hulley et al., 2017). Initial validation (Coll et al., 2016; Malakar and Hulley, 2016) and uncertainty simulations (Hulley et al., 2012) of this approach have shown accuracies at the ~ 1 K level consistently over all land cover types and atmospheric conditions.

> Read full chapter

REMOTE SENSING FOR ENVIRONMENTAL MONITORING

A.R. HUETE, in Environmental Monitoring and Characterization, 2004

DROUGHT

Combining land surface temperatures (T_s) with VIs is of great interest in drought monitoring and plant stress detection. When soil moisture is abundant, plants are able to transpire water at maximal rates for the given meteorological conditions as their leaf temperatures are generally cooler than the surrounding air temperature. As the soil dries, it becomes more difficult for plants to extract the necessary water to meet atmosphere evaporative demands, and transpiration is reduced, resulting in higher leaf temperatures than for those plants with ample water supply. A deficit of soil moisture during critical periods of the growth cycle can result in significant reductions in forage yields and net primary production and an increase in fire risk. Improved remote sensing from satellites, as well as the use of thousands of daily *in situ* precipitation measurements, has dramatically improved drought-monitoring capabilities.

Future global soil moisture and drought monitoring systems will consist of some combination of *in situ*, model estimates, and derived estimates from satellite remote sensing. Satellite thermal imagery combined with NDVI has demonstrated direct relationships between sea surface temperature variations in the Atlantic and Pacific Oceans and large-scale atmospheric circulation patterns that bring moisture or drought conditions.

> Read full chapter

Land-Surface Temperature and Thermal Infrared Emissivity

In Advanced Remote Sensing, 2012

8.4 LSE and LST Products

Sections 8.2 and 8.3 describe LST and LSE retrieval algorithms. Despite the large number of available algorithms, few algorithms are able to retrieve LST and LSE on a large scale and thereby generate LST and LSE products. As a result of complex and variable land-surface conditions, the accuracy of assumptions and approximations related to these algorithms is challenged. Typically, the assumptions and approximations established on a local scale are false at larger scales. Additionally, algorithm complexity and operational efficiency are the major factors limiting the generation of products on the large scale. Tables 8.7 and 8.8 list typical LST and LSE products and their characteristics.

TABLE 8.7. Typical LST Products

Product name	Sensor	Retrieval algorithm	Spatial resolution	Temporal resolution	Spatial coverage	Temporal coverage
MODIS LST⬚	MODIS/EOS	Split-window algorithm-Day/night algorithm	1 km/6 km	1 d	Global	2000-present
AVHRR LST	AVHRR/NOAA	Split-window algorithm	8 km	1 d	Africa	1995-2000
AVHRR LST	AVHRR/NOAA	Split-window algorithm	1.1 km	1 d	Global	1998-2007
AATSR LST	AATSR/ENVISAT	Split-window algorithm	1 km	3 d	Global	2004-present
ASTER LST	ASTER/TERRA	TES	90 m	16 d	Global	2000-present
MVIRI LST	MVIRI/METEOSAT	Neural network	5 km	30 min	Europe/Africa	1999-2005
SEVIRI LST	SEVIRI/MSG	Split-window algorithm	3 km	15 min	Europe/Africa/South America	2006-present

TABLE 8.8. Typical LSE Products

Product's name	Sensor	Retrieval algorithm	Spatial resolution	Temporal resolution	Spatial Coverage	Temporal Coverage
MODIS LSE	MODIS/EOS	Day/night algorithm	6 km	1 d	Global	2000–present
ASTER LSE	ASTER/TERRA	TES	90 m	16 d	Global	2000–present

 GLASS LSE is a broadband emissivity product in the 8–13.5 and 3–14 μm windows that is retrieved from the AVHRR and MODIS visible and near-infrared products.

Only the basic MODIS LST products are listed. Other types of LST products can be derived from the basic products. For more details, please refer to https://lp-daac.usgs.gov/lpdaac/products/modis_products_table.

> Read full chapter

Optical Remote Sensing in Urban Environments

Xavier Briottet, … Christiane Weber, in Land Surface Remote Sensing in Urban and Coastal Areas, 2016

1.2.3.3 Land surface temperature in urban areas

Obtaining the land surface temperature, LST in urban environments is linked to the acquisition geometry of the 3D structure of the scene. Furthermore, the temperature measured for an urban area shows significant daily directional effects, due to a city's high thermal heterogeneity (surfaces in shadow or in sunlight) and the directional properties of urban materials [LAG 04]. These phenomena are illustrated in Figure 1.19 which shows two temperature maps obtained using the TES algorithm [GIL 98] for two acquisitions of the AHS sensor during the ESA mission DESIREX 2008 [SOB 13], over the city of Madrid. The spatial resolution of the maps is 4 m and the AHS device has a field of view of 90°. Figure 1.19 corresponds to an acquisition carried out from the North West (NW) to the South East (SE) and Figure 1.19(b) corresponds to an acquisition across the same region but along the South (S) – North (N) axis. Both were acquired around midday local time with the second carried out at an interval of 20 min in relation to the first. There is a difference in temperature between the two maps, caused by the different surfaces viewed by the sensor depending on their position in relation to the sun. More shadows are observed when the city is covered in a NW to SE direction than when it is covered in an S to N direction. However, toward midnight, with the same acquisition configurations, any difference between the two flight lines disappears (Figure 1.20). This shows that it is easier to analyze urban environments at night in order to study urban heat islands [SOB 12b].
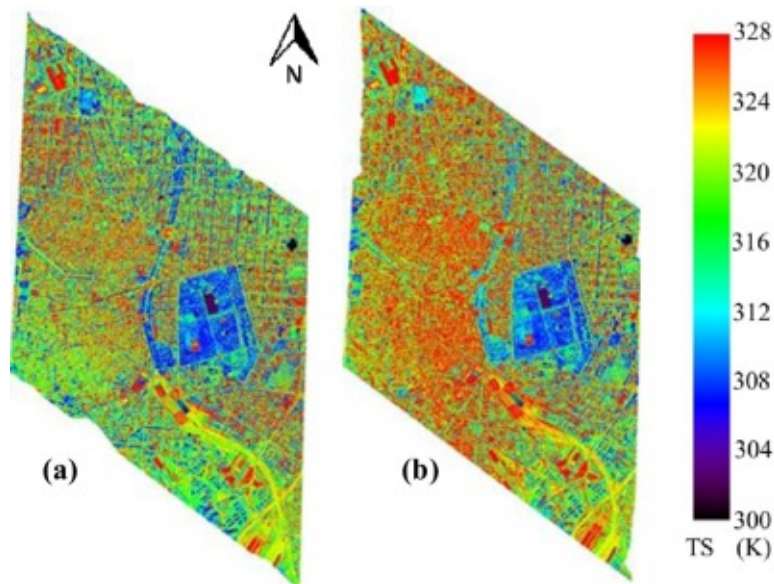
Figure 1.19. Land surface temperature maps for the same area of Madrid at midday: a) transect from NW to SE; b) transect from S to N [OLT 13]. For a color version of this figure, see www.iste.co.uk/baghdadi/5.zip
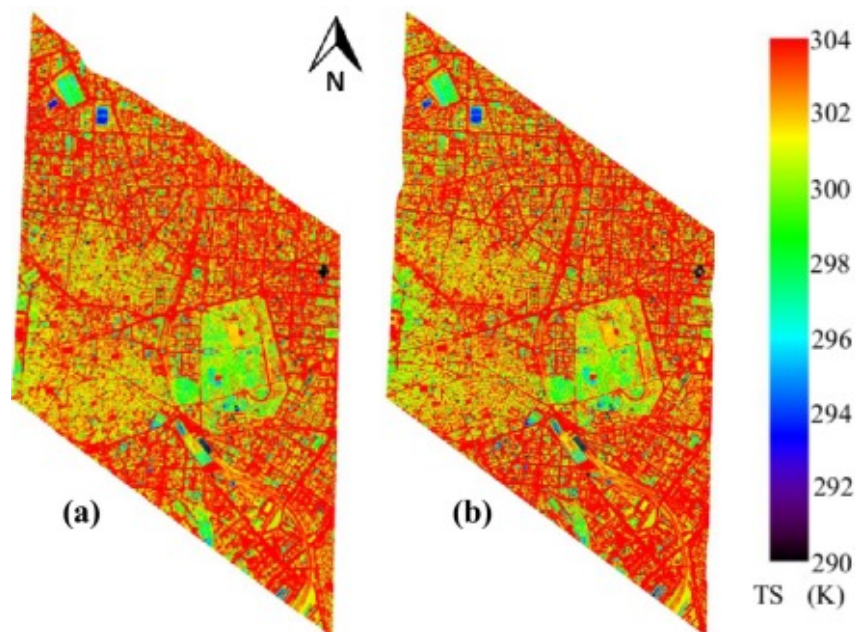

Figure 1.20. Land surface temperature maps for the same area of Madrid at midnight: a) transect from NW to SE; b) transect from N to S [OLT 13]. For a color version of this figure, see www.iste.co.uk/baghdadi/5.zip

The SUHI effect is studied in the bibliography using satellite and airborne sensors. One example of an airborne mission is the DESIREX mission, where the SUHI for Madrid is characterized during the summer with a maximum of 5 K [SOB 13].

The satellite devices currently in use do not possess a spectral or spatial resolution adapted to studying urban environments. However, they do offer a more cost-effective alternative to airborne acquisitions and are capable of providing temporal monitoring of the SUHI. Thus, the device MODIS, with a spatial resolution in the LWIR frequency of 1 km, was used by Bonafoni et al. [BON 15] in order to monitor

the evolution of SUHI for the city of Milan (Italy) over the course of a day, using four MODIS acquisitions per day. A difference of more than 4 K can be observed between the diurnal and nocturnal SUHI. Various studies using ASTER images (a spatial resolution of 90 m and five spectral bands in the LWIR frequency) have also been carried out in order to characterize the SUHI, an example of which is shown in Figure 1.21. This image shows a temperature map for Madrid at night, where the city can be identified by its high temperatures (in red) compared to the surrounding area. In [TIA 08], LST maps obtained with ASTER at night are compared to air temperature measurements for Grand Manilla (Philippines). The maximum SUHI registered there is 3 K and there is a linear correlation between LST and air temperature, with a correlation coefficient of 0.55.
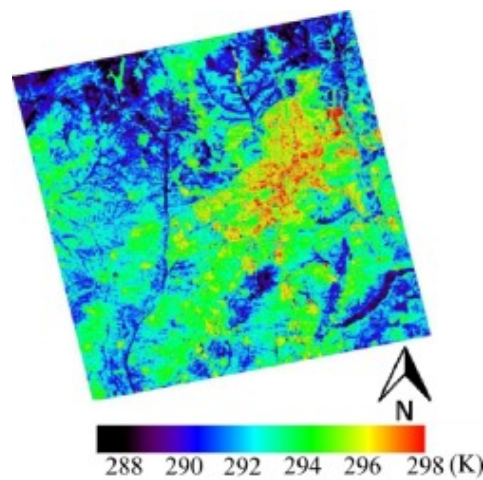

Figure 1.21. Land surface temperature map for the night of 4 July 2008 obtained using the TES algorithm [GIL 98] using an ASTER image of the city of Madrid and its surrounding area. The SUHI effect can be observed [OLT 13]. For a color version of this figure, see www.iste.co.uk/baghdadi/5.zip

Atmospheric UHI is characterized by higher levels at night and very weak, sometimes negative, levels (urban cooling islands) during the day, due to the shadows caused by buildings and urban vegetation. In the case of SUHI, we are able to note the same results for other cities such as Athens [STA 09] or Madrid [SOB 13]. However, SUHI does not always show this dynamic and it is possible to find examples where SUHI is more intense during the day than at night [BON 15]. Furthermore, this dynamic can change during the year, because the effect is linked to land cover. Even if there is no remarkable change to urban surfaces over a year, this is not the case for the surrounding areas of cities where agricultural activity, for example, can bring about seasonal changes in the surface cover. Figure 1.22 gives an example of this dynamic for the city of San Miguel de Tucuman (Northwestern Argentina), with the SUHI calculated using Landsat TM images at 2 pm UTC [OLT 10]. We were able to observe a positive SUHI during the summer and a negative SUHI during winter and spring, with these results caused by crop conditions around the city, particularly sugar cane. During September, October and November, when the SUHI is negative,

the proportion of bare ground in the pixels which cover sugar cane crops is higher than during January, February and March, when sugar cane leaves are greener and more developed. As a result, for the first case, the rural surface at 2 pm is warmer than the urban surface, while for the second case the inverse is true.
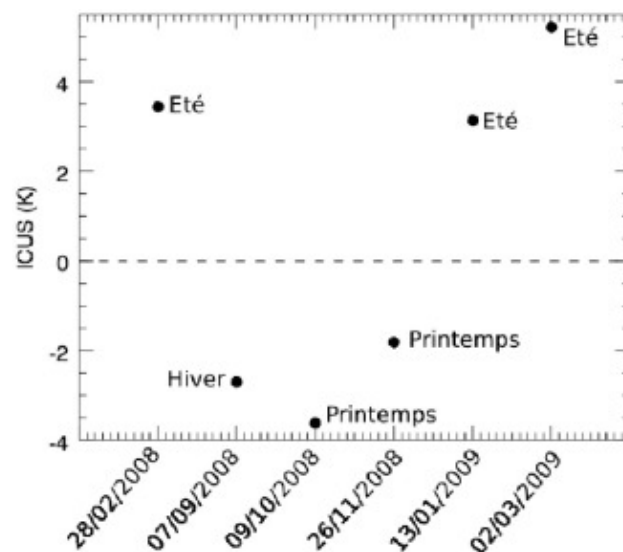

Figure 1.22. SUHI measured using Landsat TM images (2 pm UTC) for the city of San Miguel de Tucuman (Argentina) [OLT 10]

> Read full chapter

Soil Moisture Deficit Estimation Through SMOS Soil Moisture and MODIS Land Surface Temperature

P.K. Srivastava, ... R. Prasad, in Satellite Soil Moisture Retrieval, 2016

2.3 Land Surface Temperature From MODIS Satellite

The MODIS Terra satellite LST obtained through MODIS Land Processes Distributed Active Archive Center (LP DAAC) (https://lpdaac.usgs.gov/) is used in this study. The MODIS LST products are archived in Hierarchical Data Format-Earth Observing System (HDF-EOS) format files. The LST product files contain global attributes (metadata) and scientific data sets arrays with local attributes (Wan, 2006). It has a viewing swath width of 2330 km and measuring signals in 36 spectral bands between 0.405 and 14.385 μm. Due to its daily temporal resolution and free near-real time data availability, it has been selected among other operational optical/infrared satellites. The MODIS Level 3 (~ 5.6 km) LST data are gridded uniformly across the globe and used in this study for LST estimation. The Brue boundary is used for subsetting the MODIS LST global data sets using the environment for visualizing

images ITT version 4.8. A total of five pixels are extracted from the MODIS global image covering the whole Brue catchment. To use the MODIS LST it is averaged and a time series is created which is then used as an input in ANFIS for the SMD estimation. As both SMOS and MODIS come under low Earth orbiting satellites, they have local equatorial crossing times of approximately 6:00 am/6:00 pm in the case of SMOS, and 10:30 pm/10:30 am for Terra, in ascending/descending nodes. In this study, SMOS descending passes are combined with MODIS Terra ascending passes with the assumption that the soil moisture pattern is spatially persistent for a few hours before and after the SMOS overpass (Sánchez-Ruiz et al., 2014).

> Read full chapter